# Geophysical Research Letters®

**Key Points:**

- We assimilate atmospheric temperature profiles from Emirates Mars Mission-Emirates Mars InfraRed Spectrometer (EMM-EMIRS) over a 79-sol period in Mars Year 36 shortly before northern summer solstice
- EMIRS' near-hemispheric spatial coverage is used to analyze complete weather systems; we deduce the structure and motion of a warm front
- The horizontal wind diurnal cycle is retrieved by assimilation based on EMM-EMIRS' extended local time coverage of atmospheric temperatures

**Supporting Information:**

Supporting Information may be found in the online version of this article.

**Correspondence to:**

R. M. B. Young,
roland.young@uaeu.ac.ae

**Author Contributions:**

**Conceptualization:** Roland M. B. Young, François Forget
**Data curation:** Michael D. Smith, Christopher S. Edwards, Nathan Smith, Saadat Anwar, Michael J. Wolff
**Formal analysis:** Roland M. B. Young

# First Assimilation of Atmospheric Temperatures From the Emirates Mars InfraRed Spectrometer

Roland M. B. Young[1] [iD], Ehouarn Millour[2] [iD], François Forget[2], Michael D. Smith[3] [iD], Mariam Aljaberi[1], Christopher S. Edwards[4] [iD], Nathan Smith[4] [iD], Saadat Anwar[5], Philip R. Christensen[5], and Michael J. Wolff[6] [iD]

[1]Department of Physics, National Space Science and Technology Center, UAE University, Al Ain, United Arab Emirates, [2]Laboratoire de Météorologie Dynamique (LMD/IPSL), Sorbonne Université, ENS, PSL Research University, École Polytechnique, Institut Polytechnique de Paris, CNRS, Paris, France, [3]NASA Goddard Space Flight Center, Greenbelt, MD, USA, [4]Department of Astronomy and Planetary Science, Northern Arizona University, Flagstaff, AZ, USA, [5]School of Earth and Space Exploration, Arizona State University, Tempe, AZ, USA, [6]Space Science Institute, Boulder, CO, USA

**Abstract** We assimilate atmospheric temperatures from the Emirates Mars Infrared Spectrometer on board the Emirates Mars Mission (EMM) into the Mars Planetary Climate Model at the start of EMM's early science phase (Mars Year 36 $L_s = 57.34–92.90°$). Mars data assimilation benefits significantly from EMM's unique near-hemispheric observations, frequent repeated observations of the same location, and full diurnal cycle coverage. Our analysis verifies well against in-sample temperature observations, and is 1–3 K warmer than Mars Climate Sounder observations. We identify a warm front in concurrent Emirates eXploration Imager observations by correlating an elongated water ice cloud with temperatures and winds in the analysis; the analysis winds are consistent with its observed motion. We also calculate the full horizontal wind diurnal cycle; the zonal flow is weaker and the meridional circulation is stronger than simulating the same time period using the model alone.

**Plain Language Summary** The Emirates Mars Mission (EMM) promises advances in our understanding of Mars' atmosphere similar to when geostationary satellites first observed Earth. Data assimilation is a process where we combine observations with an atmospheric simulation. Using it to study Mars will benefit from EMM's observations of the whole of one side of the planet, frequent repeated observations of the same location, and observations of the full day-night cycle. We combined observations of Mars atmospheric temperatures with our model over 79 Martian days at the start of EMM's main study period. We were able to demonstrate what is possible with EMM that has not been possible before. In particular, we found a long water ice cloud near the north pole in separate visible and ultraviolet images made by EMM. By comparing the motion and structure of this cloud with our results, we found that this "warm front" also appears in our results, and we were able to deduce properties of the front that were not observed. We were also able to deduce how Martian winds change over the course of the day and night, by making use of EMM's temperature observations over the full day-night period.

## 1. Introduction

In atmospheric science, major advancements are often made when new types of instrument come online (e.g., Witschas et al., 2020), or instruments observe a planet in new ways (Kleinböhl et al., 2009). Mars' lower atmosphere and climate is controlled by seasonal and diurnal forcing, the dust cycle, water clouds, and interactions between the atmosphere and surface, among other processes (Haberle et al., 2017). Our understanding of Mars' atmosphere has come from numerical simulations (Forget et al., 1999; Richardson et al., 2007) and from satellite and surface observations (James et al., 2017), but these observations have many gaps compared with observations of Earth (Hersbach et al., 2019). A full understanding of Mars' atmosphere requires systematic observation with complete spatial and temporal coverage.

On Earth, a major leap forward in atmospheric science was made with the first geostationary meteorological satellites (Emery & Camps, 2017). These view the whole of one hemisphere systematically, tracking planetary-scale weather structures as they develop in a way that is not possible from low orbit. Nearly all Mars orbiters have been in low orbits, observing a restricted range of local times of day over a small area of the planet (James et al., 2017). This is balanced against the higher spatial resolution possible from such orbits. Large gaps remain,

particularly in our coverage of the diurnal cycle, and some quantities such as winds are not observed at all (Guzewich et al., 2020).

The Emirates Mars Mission (EMM, Amiri et al. (2022)) is unique because of its high orbit (19,970 and 42,650 km periapsis and apoapsis altitudes) and long orbital period (54.5 hr) (Almatroushi et al., 2021). Combined with its low inclination (~25°), EMM can observe almost the whole of a Martian hemisphere at once, make repeat observations a couple of hours apart or less, and observe a wide range of local times of day simultaneously. The full diurnal cycle is sampled in 9–10 days (Almatroushi et al., 2021), several times faster than was previously possible using the ExoMars Trace Gas Orbiter (TGO, Korablev et al. (2018)). This new view of Mars' atmosphere will lead to advances similar to those made with geostationary satellites for Earth.

Observational gaps in EMM's coverage of Mars' atmosphere can be filled in using data assimilation. This approach produces complete "analyses" consistent with our best theoretical understanding, encoded in a numerical model, and with what observations allow. The model passes information from observation-rich to observation-poor regions, and retrieves unobserved quantities by forcing them toward values consistent with associated observed quantities, via the model's internal balance (Kalnay, 2003). For Mars, the current state-of-the-art is to assimilate temperature and aerosol optical depths from 1 to 3 spacecraft in low polar orbit (Greybush et al., 2019; Holmes et al., 2020; Montabone et al., 2014; Ruan et al., 2021). This is a data-poor situation, particularly in the spatial and local time domains. Assimilating EMM observations is a major step forward in obtaining a global atmospheric view of Mars, and is an important part of the mission's scientific objectives (Almatroushi et al., 2021).

In this paper we present the first assimilation of atmospheric temperatures from EMM's Emirates Mars InfraRed Spectrometer (EMIRS) into the Mars Planetary Climate Model (Mars PCM), a Global Climate Model (GCM) formerly known as the Laboratoire de Météorologie Dynamique Mars Global Climate Model (LMD Mars GCM). The assimilation covers the initial period of observations during early Mars Year (MY) 36, before conjunction in 2021. The aims of this paper are to demonstrate the assimilation of near-hemispheric observations, show how complete coherent atmospheric structures can be assimilated, and how assimilating EMIRS observations fills in the gaps in the diurnal cycle. Section 2 describes the observations, Section 3 the model and assimilation method, Sections 4–6 present our results, and in Section 7 we conclude.

## 2. Observations

EMIRS is a thermal infrared spectrometer that measures radiance spectra in nadir and off-nadir geometry (0–70° emission angle) between 6 and 100 μm (Edwards et al., 2021). Vertical profiles of atmospheric temperature, among other quantities, are retrieved from these spectra as described by Smith et al. (2022).

We assimilate EMIRS atmospheric temperature retrievals from MY36 $L_s$ = 57.34–92.90°, or 11 June 2021–31 August 2021. In the model this period is between MY36 sols 121–200 (in "GCM world" time, where sol zero starts with midnight at longitude zero). This period was chosen as it provides continuous observation, after which there are some gaps mainly due to Mars conjunction. The data set contains 87,572 atmospheric temperature profiles in 542 mosaics, each mosaic typically containing 100–200 observations covering most of a hemisphere, made over 8–15 min. Temperatures are retrieved on 19 sigma levels between 0.25, 0.5, …, 4.75 scale heights above the ground, approximately one level every 2.5 km up to 47.5 km altitude. The vertical resolution of each profile is about 10 km. There is one mosaic about every 3 hr, and there is a several-hour gap every orbit when the Sun-EMM-Mars angle is too close to 0° (Amiri et al., 2022).

There is complete coverage in Local True Solar Time (LTST) between latitudes ±30°, and good coverage up to ±70° everywhere except northern hemisphere 3–10 p.m., and southern hemisphere 3–10 a.m. (Figure S1 in Supporting Information S1). During the first half of the day observations reach the north pole, and during the second half of the day they reach the south pole. The same area is continuously observed for 8–12 hr north of 45°S (Figure S2 in Supporting Information S1), and 5–8 hr elsewhere. The gap between these observation periods is 20–30 hr equatorward of 60° latitude, and 30–50 hr elsewhere.

We estimated the observational uncertainty based on pre-flight estimates (Badri et al., 2018) and the retrieval process (Smith et al., 2022). It is set to 4 K below one scale height, 2 K for 1–3 scale heights, 4 K for 3–4 scale heights, and 10 K for 4–5 scale heights.

## 3. Model and Assimilation

We assimilate observations into the Mars PCM, formerly the LMD Mars GCM (Forget et al., 1999, 2022) using the Local Ensemble Transform Kalman Filter (LETKF, Hunt et al. (2007)) with a 36-member ensemble. The GCM solves the hydrostatic primitive equations on a rotating planet, with parameterisations of radiation, diurnal, and seasonal cycles, dust and water cycles, boundary layer, subsurface, aerosols, upper atmosphere, and other relevant processes. We run the model at $5.625° \times 3.75°$ horizontal grid spacing with 32 vertical levels between 4 m and ~100 km altitude.

Our assimilation method is described in full detail by Navarro et al. (2017) and Young et al. (2022). We begin the assimilation with an ensemble whose members differ only in their visible column dust optical depth $\tau$, which is linearly spaced in log $\tau$ between 0.05 and 1.5 and set constant everywhere. This spans the realistic range of possibilities based on dust variability since MY24 (Montabone et al., 2015). This ensemble is spun up from an equilibrated atmospheric state at $L_s = 30°$.

The assimilation proceeds in 3-hr cycles. At each analysis time, observations are assimilated within a window 1.5 hr forwards and backwards from the analysis time. The forecast ensemble is used to compute the background error covariance matrix. The assimilation uses adaptive covariance inflation, and localisation with internal horizontal and vertical correlation scales of 600 km and $0.2 \ln p$ respectively. The analysis ensemble is then integrated using the GCM to produce a forecast at the next analysis time.

We use temperature observations to update the temperature field, but also use the Kalman gain computed by comparing the temperature forecast with observations to update the zonal and meridional velocities, surface pressure, and dust mass mixing ratio and number. This configuration is labeled temperature-updates-temperature-and-dust (TuTD). We exclude dust observations from the assimilation, as EMIRS dust retrievals were not yet available when we ran the assimilation. Young et al. (2022) found that assimilating the dust column produces a more accurate assimilation than TuTD during dusty periods, but our $L_s$ range is the least dusty part of the year, so we do not expect this to significantly impact our results.

For comparison, we run an ensemble of GCM simulations alongside the assimilation. This has the same size and initialization as the LETKF ensemble, but during the assimilation period no observations are assimilated, and dust is constrained by a "dust scenario" (Montabone et al., 2015) based on daily maps of column dust optical depth using Mars Reconnaissance Orbiter — Mars Climate Sounder (MRO-MCS) observations for MY36. This is the standard mode for the Mars PCM.

The observation operator compares the forecast with each retrieval within the assimilation window. First we linearly interpolate the forecast to the retrieval's horizontal location and time. Then, because the instrument is a nadir sounder, and its vertical resolution is lower than the model's vertical grid spacing, it is necessary to smooth the forecast profile to reproduce what the instrument would measure if it observed the forecast atmosphere. We apply a vertical convolution similar to that used for the Mars Global Surveyor — Thermal Emission Spectrometer (MGS-TES) by Conrath et al. (2000), from which EMIRS derives significant heritage. At each vertical position $Z_k = -\ln \sigma_k$, $k = 1 \dots K$, measured in scale heights above the surface, an effective forecast temperature profile $T_k^{\text{eff}}$ is generated by convolving the forecast $T_k$ with a Gaussian peaking at $Z_k$, with correlation length $c = 0.75$ scale heights. The resulting smoothed profile of effective temperature is

$$T_k^{\text{eff}} = \left( \sum_{j=1}^{K} T_j w_j^k \Delta Z_j \right) \Big/ \left( \sum_{j=1}^{K} w_j^k \Delta Z_j \right) \tag{1}$$

Each effective temperature $T_k^{\text{eff}}$ is assigned an effective altitude $Z_k^{\text{eff}}$. This is because the effective temperature is a weighted average, and hence the corresponding vertical location must be the same weighted average of the profile altitudes:

$$Z_k^{\text{eff}} = \left( \sum_{j=1}^{K} Z_j w_j^k \Delta Z_j \right) \Big/ \left( \sum_{j=1}^{K} w_j^k \Delta Z_j \right) \tag{2}$$
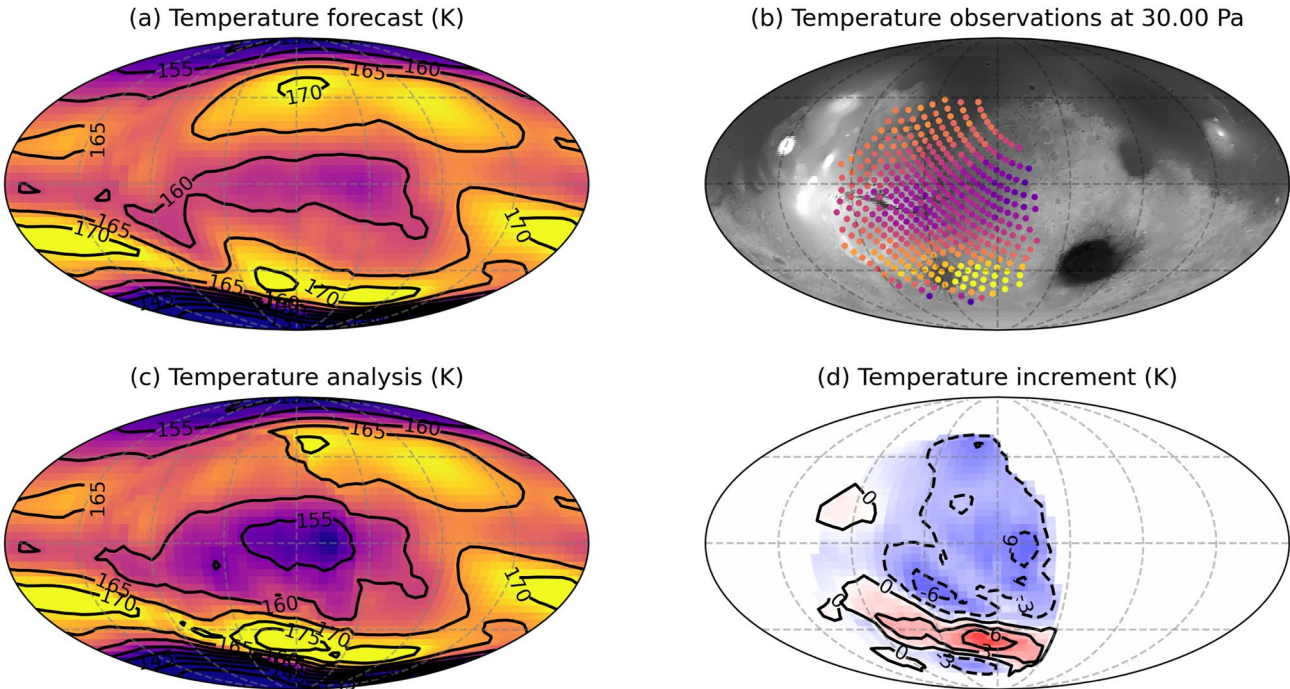
**Figure 1.** Example temperature fields from assimilation of Emirates Mars InfraRed Spectrometer atmospheric temperatures. Data are interpolated vertically to 30 Pa, linearly in log $p$. (a) Atmospheric temperature forecast, with contours separated by 5 K. (b) Atmospheric temperature profiles within the assimilation window (analysis time $\pm 1.5$ hr), using the same colors as (a); 90% of the observations are between 2.5 and 3.3 scale heights above the surface. The background uses Mars Orbiter Laser Altimeter (MOLA) data (Smith et al., 2001). (c) Atmospheric temperature analysis. (d) Temperature increment (analysis minus forecast), with contours separated by 3 K. Each figure is a Mollweide projection centered on longitude/latitude zero. The analysis/forecast data are from MY36 sol 165.75 ($L_s = 77.50°$). The Local True Solar Time at longitude zero is 18:00. Figure S4 in Supporting Information S1 shows equivalent plots for wind.

Here $\Delta Z_j$ is the thickness of level $j$ in scale heights, and $w^k$ is the smoothing function for level $k$, a Gaussian centered on $Z_k$:

$$w_j^k = \exp\left[-\frac{(Z_j - Z_k)^2}{2c^2}\right] \tag{3}$$

$Z^{\text{eff}}$ is always positive, so $T^{\text{eff}}$ does not reach the ground (its minimum, for $Z_k = 0$, is $c\sqrt{2/\pi} \approx 0.60$). We then sample the effective forecast profile at the same vertical positions as the retrieval, and compare these forecast temperatures directly against the temperature retrieval. The lowest position in the effective temperature profile is at $Z = 0.75$ scale heights. Figure S3 in Supporting Information S1 shows an example forecast temperature profile with the smoothed profile and sampled temperatures for comparison with the retrieval.

## 4. Assimilation of Hemispheric Observations

Figure 1 shows an example atmospheric temperature analysis produced by assimilating EMIRS atmospheric temperature profiles into the model. Assimilating EMIRS observations updates the atmospheric state over a large area of the planet simultaneously. The observed temperatures are densely packed and spatial variations are smooth. The observation density is close to the GCM grid spacing, while still covering an area 90–135° in diameter. Observations from polar orbiters have higher data density, but this can be sub-optimal due to over-sampling, requiring pre-processing into "superobservations" to reduce representativeness and instrument errors (see Greybush et al. (2019) for an example using TES and MCS). With EMIRS this is not necessary.

The assimilation behaves well and is generally stable, more so than earlier work using TGO observations (Young et al., 2022). This is for two reasons. First, with EMIRS we assimilate extended atmospheric structures over a large area, which introduces fewer large gradients into the analysis (Figure 1d), and leads to less numerical instability in the subsequent forecast step. With a polar orbiter we assimilate data in a thin swathe, and sometimes this

introduces large gradients into the analysis between locations that were just updated, and locations that have not been updated for some hours. Second, our assimilation takes place when dust activity is lowest during the Martian year. We expect that, as dust concentrations increase later in MY36, the model will have to work harder to keep up with day-to-day changes due to interactions between dust and the thermal environment.

We calculated the forecast and analysis temperature bias and root-mean-squared (RMS) error compared with in-sample EMIRS temperature profiles and independent MCS temperature profiles. Figures S5 and S6 in Supporting Information S1 show time series, and Table S1 in Supporting Information S1 shows summary statistics.

The bias compared with EMIRS falls from 1 to 2 K in the forecast to nearly zero in the analysis, and the RMS error falls from 3–5 K to 2 K. We do not expect the RMS error to fall below the estimated EMIRS uncertainty of 2 K. Both statistics demonstrate that the assimilation reduces the distance between the model state and reality; a strong reason to use the analysis over the model or observations alone in subsequent analyses of specific phenomena.

Verification against MCS shows larger errors and smaller differences between forecast and analysis, as expected. There is a small reduction in the analysis bias compared with the forecast. Our analysis is typically 1–3 K warmer than MCS, with a RMS error between 5 and 7 K. The GCM ensemble performs better than the assimilation when compared with MCS because it is constrained by MCS dust observations, which will still make some difference even though this time of year has low dust levels.

## 5. Coherent Weather Structures

One of the most powerful aspects of data assimilation is to retrieve quantities that cannot be observed, such as winds in the case of Mars. Both Figures 2 and 3 illustrate this point. To demonstrate the assimilation of coherent weather structures, Figure 2 shows an example identified in EMM Emirates eXploration Imager imaging (EXI, Jones et al. (2021)), and our corresponding LETKF analysis.

We searched the EXI ultraviolet 320 nm images for examples containing water ice clouds indicative of atmospheric fronts or vortices, and in visible images for similar dust features. We identified 23 such observations during the assimilation period, many with dust or cloud NW or NE of Alba Mons. The best example was captured in eight observations over four hours on 16 August 2021 ($L_s = 86.29–86.34°$). The final three observations suffered from some pointing errors, so we focused on the first five. All eight observations are listed in the Supporting Information S1, along with animations of the sequence. These observations show an elongated water ice cloud above Acidalia Planitia, 3–5° wide and ∼60° long. To the north is a vortex-like dust feature 20–25° in diameter. Figure 2 shows our best view of this feature (Figures 2a and 2b), along with a close-up of the water ice cloud showing its northwestward motion over 2.5 hr (Figure 2d), and vertical sections through the temperature and wind analysis fields perpendicular to the cloud (Figure 2e). Emirates Mars Infrared Spectrometer has decent coverage of this area during the sequence (Figure 2c).

The water ice cloud's shape suggests an atmospheric front is present in this region. Our LETKF analysis is consistent with this interpretation. Temperatures have a weak maximum around 25–30°N, characteristic of the season (Figure 2a), and winds are mainly between N and W in the northern hemisphere. Locally, the temperature field contains a steep gradient poleward of the water ice cloud, with a temperature decrease of 10 K over 20–25° (Figure 2b), and the wind blows across the water ice cloud toward the N or NW. Flow from warm to cold downwind of a water cloud is characteristic of a warm front (Sawyer, 1956). The vertical structure perpendicular to the temperature contours (Figure 2e) shows a temperature inversion, with warm air above and south of cooler air, a strong horizontal temperature gradient, flow with a component perpendicular to the cloud upwind and downwind of the temperature gradient, and upwards flow at and downwind of the cloud. These are all consistent with a northwestward-propagating warm front, and suggest that the water ice cloud has formed due to adiabatic cooling associated with synoptic-scale ascent.

We estimated the wind speed and direction within the water ice cloud by comparing visible features of the water ice cloud some time apart. A more systematic analysis could be done using Correlation Imaging Velocimetry (Fincham & Spedding, 1997), but here we simply estimate the wind using three tie points manually placed on features that are visible in two or more images. The shape of the water ice cloud does not visibly evolve over this time period. The images in Figure 2d are the first and fifth in the sequence, and show the three tie points. Based
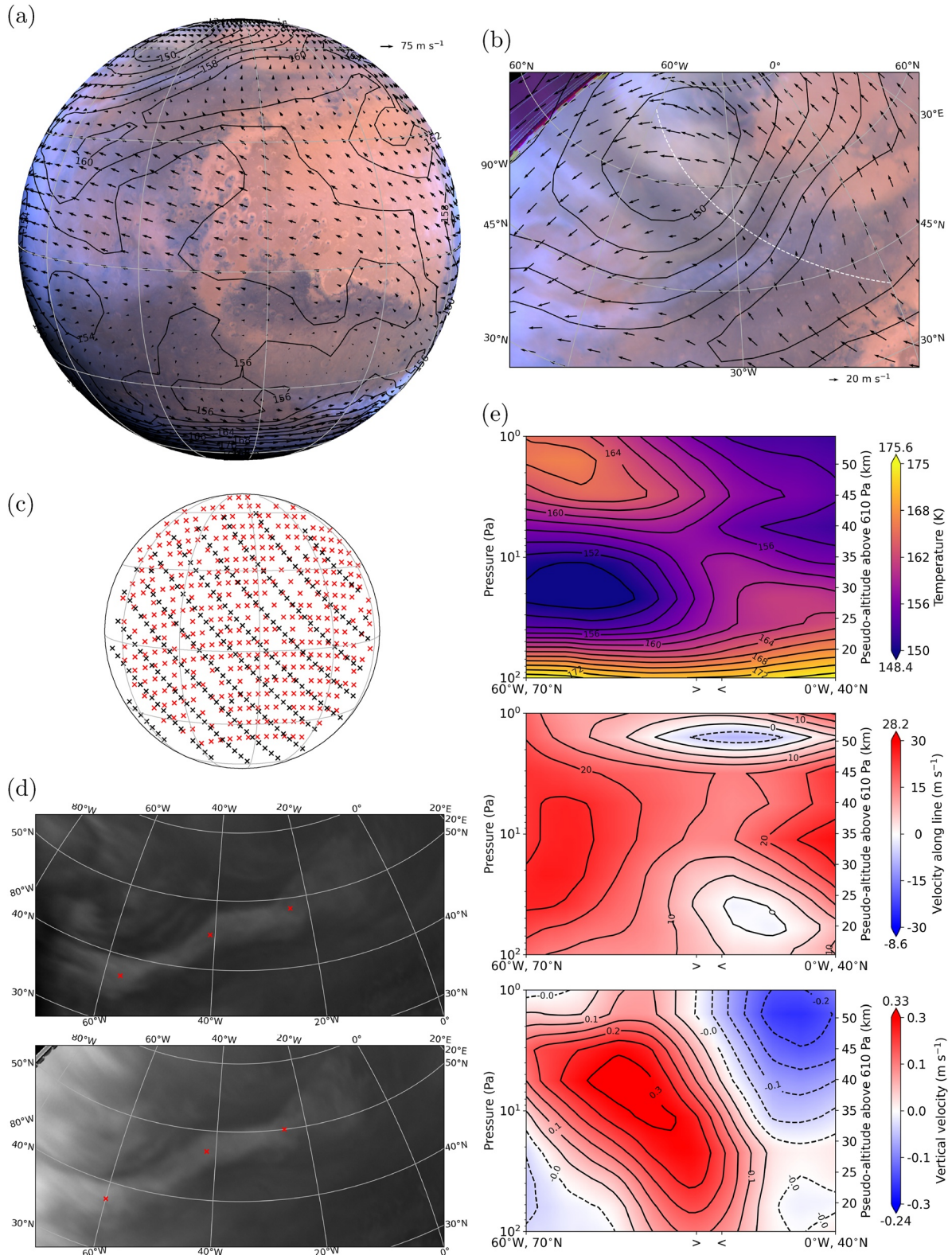
**Figure 2.**

on the motion of these points between the two images, from left to right the wind speeds are 15, 13, and 10 m s$^{-1}$, and the bearings are 283, 341, and 336°, respectively. Assuming the position of each tie point is accurate to within 0.5°, the speeds have an uncertainty of ~2 m s$^{-1}$ and the bearings ~10°. The wind vectors correspond somewhat to our LETKF analysis at the same locations and time, which have speeds 23, 12, and 9 m s$^{-1}$ and bearings 248, 256, and 355°, respectively.

## 6. Temperature and Wind Diurnal Cycles

Figure 3 shows diurnal cycles of temperature, zonal velocity, and meridional velocity in our analysis. EMIRS observations during this period are shown in Figure 3b, filling in the full range of local times at all latitudes except for short periods in northern evening and southern morning. The improvement in EMIRS' local time coverage over MCS (Figure 3c) is dramatic.

The temperature analysis shows extrema in essentially the same places and times as EMIRS observations, but with reduced magnitudes. These are reduced because the analysis is fundamentally a weighted average of the EMIRS observations and the model. Equivalent figures for the GCM ensemble are shown in Figure S7 in Supporting Information S1. The diurnal variation is larger in the analysis than in the GCM ensemble, for temperature and wind. Hence the diurnal variation in the analysis will be somewhere between the diurnal variation in EMIRS observations and in the GCM ensemble.

The temperature diurnal cycle differs in some details from the diurnal cycle in the GCM ensemble. Overall, the GCM reproduces the analysis diurnal cycle well, a testament to the quality of the model, but the amplitudes are different. In the northern hemisphere the analysis is 4 K warmer in the evening, and 2 K cooler in the morning. Near the equator, there is an isolated maximum at 2–3 a.m. missing from the GCM ensemble, and the analysis is about 2 K warmer at that time. Finally, in the southern hemisphere the temperature maximum centered on 8–9 p.m. is 2 K cooler than in the GCM ensemble, and covers a shorter local time range.

The assimilation combined with observational temperature coverage of all local times allows us to reconstruct the diurnal cycle for horizontal wind with a level of confidence that has not been possible before. Figures 3d and 3e show the diurnal cycle for the zonal and meridional velocity. There is a strong eastward zonal jet in the southern hemisphere whose amplitude is strongest in the late evening (100–110 m s$^{-1}$) and weakest at noon (70–80 m s$^{-1}$). In the equatorial region, the zonal wind is retrograde with the strongest wind (40–50 m s$^{-1}$) between 3 a.m. and 1 p.m., and the weakest at 9 p.m. (10–20 m s$^{-1}$). In the northern hemisphere there is 40–50 m s$^{-1}$ eastward flow in the evening and 0–10 m s$^{-1}$ in the morning, reversing at some latitudes. Sub-diurnal periodicities in the zonal velocity are too weak to be detected in this figure.

The meridional velocity has an even stronger diurnal cycle, and also lacks significant sub-diurnal periodicities. The meridional flow is generally poleward during the day and equatorward at night, consistent with a single Hadley cell. In the northern hemisphere the poleward flow is between 8 a.m. and 8 p.m., peaking at 30–35 m s$^{-1}$ at 1–2 p.m., which is mirrored in direction and amplitude at other times, peaking around 1 a.m. In the southern hemisphere the poleward flow is between 10:30 a.m. and 10:30 p.m., with a weaker 20–25 m s$^{-1}$ peak around 5 p.m. It is equatorward at other times, with a peak at 20 m s$^{-1}$ around 5 a.m.

The zonal flow in the analysis is about 10 m s$^{-1}$ weaker than the GCM ensemble at most latitudes and local times. In the analysis the southern hemisphere eastward jet is 5–10° farther south than in the GCM ensemble, and is wider in latitude. Conversely, the analysis meridional velocity is about 5 m s$^{-1}$ stronger than the GCM ensemble at

**Figure 2.** A northwestward-propagating warm front above Acidalia Planitia captured in our Local Ensemble Transform Kalman Filter analysis and in concurrent Emirates eXploration Imager (EXI) imaging. (a) Analysis on top of a composite EXI RGB image (635, 546, 437 nm), as seen from Emirates Mars Mission's location. The mean solar longitude of the individual RGB images is $L_s = 86.32°$, or sol 185.47 in the analysis. The Local True Solar Time (LTST) at the sub-spacecraft point is 10:50. Black lines are temperature contours at 20 Pa, separated by 2 K, and black arrows are horizontal wind vectors at 20 Pa. (b) Inset (orthographic) showing the upper left part of (a). The white dashed line is straight in longitude-latitude coordinates. The limb is in the top left corner. (c) Location of Emirates Mars InfraRed Spectrometer observations immediately before (red, $L_s = 86.28°$) and after (black, $L_s = 86.32°$) the image in (a). (d) 320 nm EXI images showing the water ice cloud at $L_s = 86.29°$ (top) and $L_s = 86.34°$ (bottom). The Local True Solar Times at 40°W are 06:52:02 and 09:26:54, respectively. Small red crosses are used to estimate wind vectors. Brightnesses in the upper panel are increased by 25%. (e) Vertical cross-sections along the dashed white line in (b) through the analysis temperature (top), velocity along the line, positive poleward (middle), and vertical velocity (bottom). Contours are separated by 2 K, 5 m s$^{-1}$, and 0.05 m s$^{-1}$, respectively. The > < show the approximate location of the cloud. Pseudo-altitudes are estimated using a pressure scale height of 8.5 km. To highlight the vertical structure of the frontal system, the cross-sections only extend down to 100 Pa.
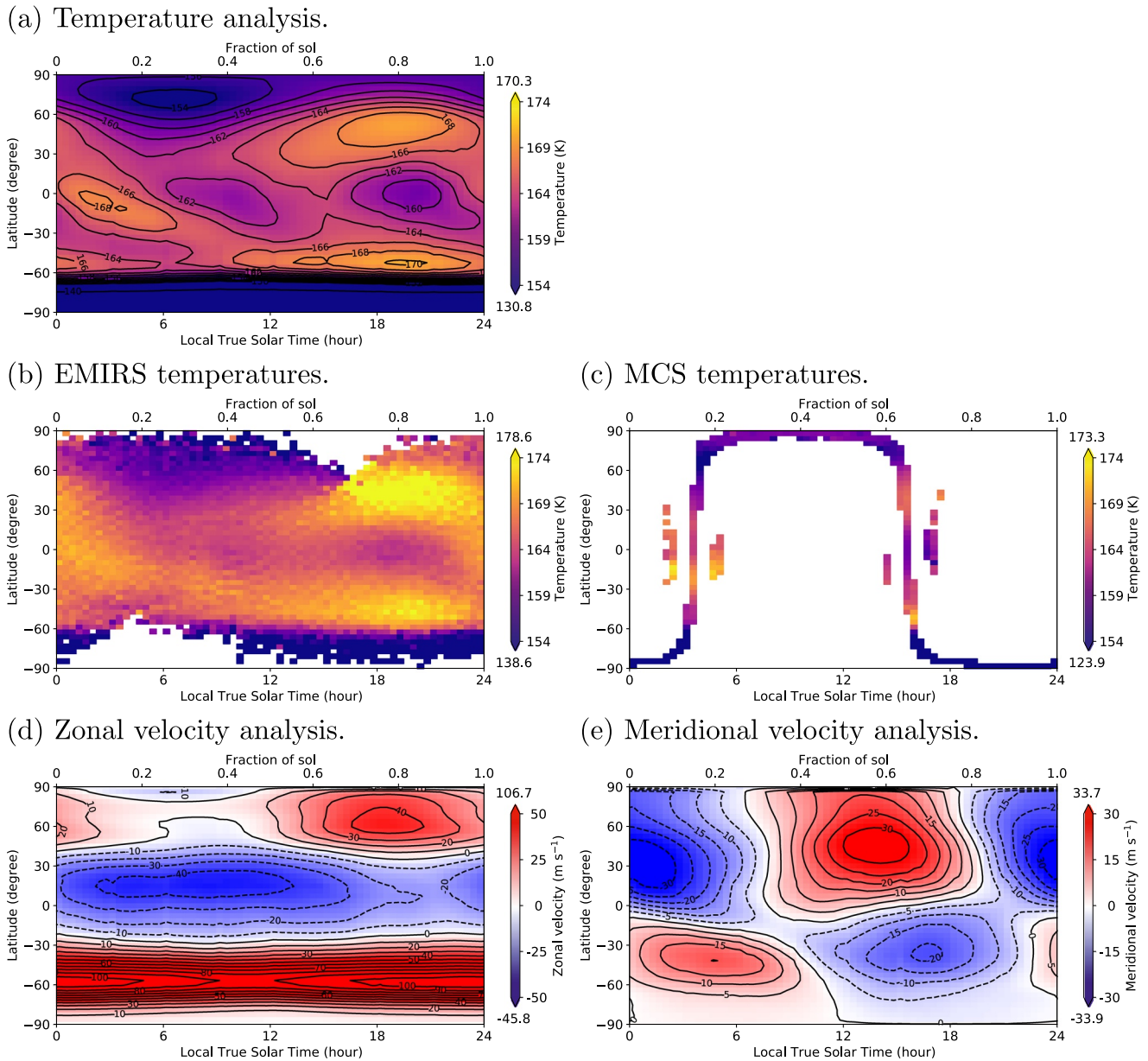
(a) Temperature analysis.



(b) EMIRS temperatures.



(c) MCS temperatures.



(d) Zonal velocity analysis.



(e) Meridional velocity analysis.



**Figure 3.** The diurnal cycle at 30 Pa, averaged over MY36 $L_s = 60$–$90°$, as a function of Local True Solar Time (LTST) and latitude. (a) Local Ensemble Transform Kalman Filter (LETKF) temperature analysis; (b) EMIRS and (c) MCS temperature profiles linearly interpolated in log $p$ to 30 Pa; (d) LETKF zonal velocity analysis; (e) LETKF meridional velocity analysis. White regions in (b and c) indicate missing data. Points are separated by 0.375 hr in local time (equivalent to one longitudinal Global Climate Model (GCM) grid box) and 3.75° in latitude (GCM latitudinal grid spacing). The analysis is interpolated in local time, and Emirates Mars InfraRed Spectrometer (EMIRS) and Mars Climate Sounder (MCS) profiles are averaged in local time and latitude bins. Numbers above and below each color bar indicate the maximum and minimum values; note the temperature color scale is compressed to enhance contrast. Contour lines are spaced by 2 K (temperature), 10 m s$^{-1}$ (zonal velocity), and 5 m s$^{-1}$ (meridional velocity).

most latitudes and local times. About 18% of the analysis kinetic energy is in the meridional flow at the end of the assimilation period, compared with 12% for the GCM ensemble. This implies that the kinetic energy may be more strongly weighted toward the meridional circulation compared with the zonal flow than is simulated by the GCM.

## 7. Conclusion

We have completed a first assimilation of EMIRS atmospheric temperatures into the Mars PCM, over the initial part of EMM's science phase up to MY36 northern summer solstice. We demonstrated some unique characteristics of EMM relevant for data assimilation.

The ability to assimilate near-hemispheric data and hence complete coherent weather structures, along with repeated observation of the same area over several hours, was demonstrated by our analysis of the structure and motion of a warm front that also appears in EXI imaging (Figure 2). Such an analysis would not have been possible from earlier spacecraft whose field of view is much smaller, and which do not repeatedly observe the same location. This also showed that we can use the assimilation to retrieve wind fields similar to observed winds. We plan to assimilate observations of other complete structures such as vortices and baroclinic waves, and the evolution of dust events.

Full local time coverage was demonstrated by our analysis of the diurnal cycles of zonal and meridional velocity (Figure 3). Our confidence in these results is high because the diurnal cycle of temperatures is almost fully sampled at all latitudes by EMIRS during this period. We found some significant differences compared with the diurnal cycle of winds predicted by GCM simulations alone.

Many parts of the data set remain to be assimilated, including surface temperatures, dust, water ice, and water vapor opacities, along with comparable observations from EXI. Like geostationary observations did for Earth, EMM has great potential to improve our understanding of Mars' atmosphere using data assimilation.

## Data Availability Statement

Data from the Emirates Mars Mission (EMM) are freely and publicly available on the EMM Science Data Center (SDC, http://sdc.emiratesmarsmission.ae). This location is designated as the primary repository for all data products produced by the EMM team and is designated as long-term repository as required by the UAE Space Agency. The data available (http://sdc.emiratesmarsmission.ae/data) include ancillary spacecraft data, instrument telemetry, Level 1 (raw instrument data) to Level 3 (derived science products), quicklook products, and data users guides (https://sdc.emiratesmarsmission.ae/documentation) to assist in the analysis of the data. Following the creation of a free login, all EMM data are searchable via parameters such as product file name, solar longitude, acquisition time, sub-spacecraft latitude and longitude, instrument, data product level, etc.

Data products can be browsed within the SDC via a standardized file system structure that follows the convention: `/emm/data/<Instrument>/<DataLevel>/<Mode>/<Year>/<Month>`

Data product filenames follow a standard convention: `emm_<Instrument>_<DataLevel><Start-TimeUTC>_<OrbitNumber>_<Mode>_<Description>_<KernelLevel>_<Version>.<File-Type)`

Emirates Mars Infrared Spectrometer (EMIRS) data and user guides are available at: https://sdc.emiratesmarsmission.ae/data/emirs.

Emirates eXploration Imager (EXI) data and user guides are available at: https://sdc.emiratesmarsmission.ae/data/exi.

The data produced by our assimilation can be obtained via the EMM SDC at https://data-sdc-publications-mbrsc.s3.eu-west-1.amazonaws.com/Young-EMIRS-assimilation-MY36-first-results.zip.

Mars Climate Sounder observations are available from the NASA Planetary Data System Atmospheres node at https://pds-atmospheres.nmsu.edu/data_and_services/atmospheres_data/MARS/mars_reconnaissance_orbiter.html.

MOLA topography data are available from the NASA Planetary Data System Geosciences node at https://pds-geosciences.wustl.edu/missions/mgs/megdr.html.

The Mars PCM is available from http://www-mars.lmd.jussieu.fr/; we used GCM subversion revision r2533. The assimilation uses letkfmars git revision 9421d1c2a78abbd03eafc2cf3c1b0719e7586660.

## References

Almatroushi, H., AlMazmi, H., AlMheiri, N., AlShamsi, M., AlTunaiji, E., Badri, K., et al. (2021). Emirates Mars Mission characterization of Mars atmosphere dynamics and processes. *Space Science Reviews*, *217*(8), 89. https://doi.org/10.1007/s11214-021-00851-6

Amiri, S., Brain, D., Sharaf, O., Withnell, P., McGrath, M., Alloghani, M., et al. (2022). The Emirates Mars Mission. *Space Science Reviews*, *218*(1), 4. https://doi.org/10.1007/s11214-021-00868-x

Badri, K., Altunaiji, E., Edwards, C. S., Smith, M. D., Christensen, P. R., Almheiri, S., et al. (2018). Scientific payload of the Emirates Mars Mission: Emirates Mars InfraRed Spectrometer (EMIRS). In *European Planetary Science Congress, Berlin* (Vol. 12, p. 1007).

Conrath, B. J., Pearl, J. C., Smith, M. D., Maguire, W. C., Christensen, P. R., Dason, S., & Kaelberer, M. S. (2000). Mars Global Surveyor Thermal Emission Spectrometer (TES) observations: Atmospheric temperatures during aerobraking and science phasing. *Journal of Geophysical Research: Planets*, *105*(E4), 9509–9519. https://doi.org/10.1029/1999JE001095

Edwards, C. S., Christensen, P. R., Mehall, G. L., Anwar, S., Al Tunaiji, E., Badri, K., et al. (2021). The Emirates Mars Mission (EMM) Emirates Mars InfraRed spectrometer (EMIRS) instrument. *Space Science Reviews*, *217*(7), 77. https://doi.org/10.1007/s11214-021-00848-1

Emery, W., & Camps, A. (2017). The history of satellite remote sensing. In *Introduction to satellite remote sensing* (pp. 1–42). Elsevier. https://doi.org/10.1016/B978-0-12-809254-5.00001-4

Fincham, A. M., & Spedding, G. R. (1997). Low cost, high resolution DPIV for measurement of turbulent fluid flow. *Experiments in Fluids*, *23*(6), 449–462. https://doi.org/10.1007/s003480050135

Forget, F., Hourdin, F., Fournier, R., Hourdin, C., Talagrand, O., Collins, M., et al. (1999). Improved general circulation models of the Martian atmosphere from the surface to above 80 km. *Journal of Geophysical Research: Planets*, *104*(E10), 24155–24175. https://doi.org/10.1029/1999JE001025

Forget, F., Millour, E., Bierjon, A., Delavois, A., Fan, S., Lange, L., et al. (2022). Challenges in Mars climate modelling with the LMD Mars Global Climate Model, now called the Mars 'Planetary Climate Model' (PCM). In *7th workshop on Mars atmosphere modelling and observations* (pp. 14–17).

Greybush, S. J., Kalnay, E., Wilson, R. J., Hoffman, R. N., Nehrkorn, T., Leidner, M., et al. (2019). The Ensemble Mars Atmosphere Reanalysis System (EMARS) version 1.0. *Geoscience Data Journal*, *6*(2), 137–150. https://doi.org/10.1002/gdj3.77

Guzewich, S. D., Abshire, J. B., Baker, M. M., Battalio, J. M., Bertrand, T., Brown, A. J., et al. (2020). Measuring Mars atmospheric winds from orbit. *Bulletin of the American Astronomical Society*, *53*(4), 35. https://doi.org/10.3847/25c2cfeb.6576a506

Haberle, R. M., Clancy, R. T., Forget, F., Smith, M. D., & Zurek, R. W. (Eds.). (2017). *The atmosphere and climate of Mars*. Cambridge University Press. https://doi.org/10.1017/9781139060172

Hersbach, H., Bell, W., Berrisford, P., Horányi, A., Sabater, J. M., Nicolas, J., et al. (2019). Global reanalysis: Goodbye ERA-Interim, hello ERA5. *ECMWF Newsletter*, *159*, 17–24. https://doi.org/10.21957/vf291hehd7

Holmes, J. A., Lewis, S. R., & Patel, M. R. (2020). OpenMARS: A global record of Martian weather from 1999 to 2015. *Planetary and Space Science*, *188*, 104962. https://doi.org/10.1016/j.pss.2020.104962

Hunt, B. R., Kostelich, E. J., & Szunyogh, I. (2007). Efficient data assimilation for spatiotemporal chaos: A local ensemble transform Kalman filter. *Physica D*, *230*(1–2), 112–126. https://doi.org/10.1016/j.physd.2006.11.008

James, P. B., Christensen, P. R., Clancy, R. T., Lemmon, M. T., & Withers, P. (2017). History of Mars atmosphere observations. In *The atmosphere and climate of Mars* (pp. 20–41). Cambridge University Press. https://doi.org/10.1017/9781139060172.003

Jones, A. R., Wolff, M., Alshamsi, M., Osterloo, M., Bay, P., Brennan, N., et al. (2021). The Emirates Exploration Imager (EXI) instrument on the Emirates Mars Mission (EMM) Hope mission. *Space Science Reviews*, *217*(8), 81. https://doi.org/10.1007/s11214-021-00852-5

Kalnay, E. (2003). *Atmospheric modeling, data assimilation and predictability*. Cambridge University Press. https://doi.org/10.1017/CBO9780511802270

Kleinböhl, A., Schofield, J. T., Kass, D. M., Abdou, W. A., Backus, C. R., Sen, B., et al. (2009). Mars Climate Sounder limb profile retrieval of atmospheric temperature, pressure, and dust and water ice opacity. *Journal of Geophysical Research: Planets*, *114*, E10006. https://doi.org/10.1029/2009JE003358

Korablev, O., Montmessin, F., Trokhimovskiy, A., Fedorova, A. A., Shakun, A. V., Grigoriev, A. V., et al. (2018). The Atmospheric Chemistry Suite (ACS) of three spectrometers for the ExoMars 2016 Trace Gas Orbiter. *Space Science Reviews*, *214*(1), 7. https://doi.org/10.1007/s11214-017-0437-6

Montabone, L., Forget, F., Millour, E., Wilson, R. J., Lewis, S. R., Cantor, B., et al. (2015). Eight-year climatology of dust optical depth on Mars. *Icarus*, *251*, 65–95. https://doi.org/10.1016/j.icarus.2014.12.034

Montabone, L., Marsh, K., Lewis, S. R., Read, P. L., Smith, M. D., Holmes, J., et al. (2014). The Mars Analysis Correction Data Assimilation (MACDA) dataset V1.0. *Geoscience Data Journal*, *1*(2), 129–139. https://doi.org/10.1002/gdj3.13

Navarro, T., Forget, F., Millour, E., Greybush, S. J., Kalnay, E., & Miyoshi, T. (2017). The challenge of atmospheric data assimilation on Mars. *Earth and Space Science*, *4*(12), 690–722. https://doi.org/10.1002/2017EA000274

Richardson, M. I., Toigo, A. D., & Newman, C. E. (2007). PlanetWRF: A general purpose, local to global numerical model for planetary atmospheric and climate dynamics. *Journal of Geophysical Research: Planets*, *112*(E9), E09001. https://doi.org/10.1029/2006JE002825

Ruan, T., Young, R. M. B., Lewis, S. R., Montabone, L., Valeanu, A., & Read, P. L. (2021). Assimilation of both column- and layer-integrated dust opacity observations in the Martian atmosphere. *Earth and Space Science*, *8*(12), e2021EA001869. https://doi.org/10.1029/2021EA001869

Sawyer, J. S. (1956). The vertical circulation at meteorological fronts and its relation to frontogenesis. *Proceedings of the Royal Society of London*, *234*, 346–362. https://doi.org/10.1098/rspa.1956.0039

Smith, D. E., Zuber, M. T., Frey, H. V., Garvin, J. B., Head, J. W., Muhleman, D. O., et al. (2001). Mars Orbiter Laser Altimeter: Experiment summary after the first year of global mapping of Mars. *Journal of Geophysical Research: Planets*, *106*(E10), 23689–23722. https://doi.org/10.1029/2000JE001364

Smith, M. D., Badri, K., Atwood, S. A., Edwards, C. S., Christensen, P. R., Wolff, M. J., et al. (2022). EMIRS observations of the aphelion-season Mars atmosphere. *Geophysical Research Letters*, *49*, e2022GL099636. https://doi.org/10.1029/2022GL099636

Witschas, B., Lemmerz, C., Geiß, A., Lux, O., Marksteiner, U., Rahm, S., et al. (2020). First validation of Aeolus wind observations by airborne Doppler wind lidar measurements. *Atmospheric Measurement Techniques*, *13*(5), 2381–2396. https://doi.org/10.5194/amt-13-2381-2020

Young, R. M. B., Millour, E., Guerlet, S., Forget, F., Ignatiev, N., Grigoriev, A. V., et al. (2022). Assimilation of temperatures and column dust opacities measured by ExoMars TGO-ACS-TIRVIM during the MY34 Global Dust Storm. *Journal of Geophysical Research: Planets*, *127*, e2022JE007312. https://doi.org/10.1029/2022JE007312

## References From the Supporting Information

Jeppesen, C., Jones, A., Shuping, R., & Wolff, M. (2021). *EXI data product guide (Document No. 169996)*. Mohammed bin Rashid Space Centre. Retrieved from https://sdc.emiratesmarsmission.ae